



Contents lists available at ScienceDirect

## International Journal of Plasticity

journal homepage: [www.elsevier.com/locate/ijplas](http://www.elsevier.com/locate/ijplas)

# Understanding thermally-activated glide of $1/2\langle 110 \rangle\{110\}$ screw dislocations in $\text{UO}_2$ – A molecular dynamics analysis

A.V. Lunev<sup>a,b,\*</sup>, S.V. Starikov<sup>a</sup>, T.N. Aliev<sup>c</sup>, V.I. Tseplyaev<sup>a</sup><sup>a</sup> Joint Institute for High Temperatures of the Russian Academy of Sciences, 13 Bld. 2, Izhorskaya St., 125412, Moscow, Russia<sup>b</sup> United Kingdom Atomic Energy Authority (UKAEA), Culham Science Centre, Abingdon, Oxfordshire, OX14 3DB, United Kingdom<sup>c</sup> State Research Centre of Russian Federation, “Troitsk Institute for Innovation and Fusion Research”, SRC RF TRINITI, Troitsk, 142190, Moscow Reg., Russia

## ARTICLE INFO

## Keywords:

Dislocations  
Ceramic material  
Numerical algorithms  
Atomistic simulation

## ABSTRACT

As shown experimentally, the interplay between screw and edge dislocations in uranium dioxide ( $\text{UO}_2$ ) determines the low-temperature plasticity in this material. For the latter, neither the mobility of screw dislocations nor the mechanisms of their glide had been assessed – up until now. It is particularly interesting to evaluate the mobility of  $1/2\langle 110 \rangle\{110\}$  screw dislocations, supposedly the least mobile in  $\text{UO}_2$  due to the allegedly extremely high Peierls barrier of their motion. To address this issue, molecular dynamics simulations of dislocation glide are conducted on Lomonosov/MVS-10P supercomputers with LAMMPS software, and post-processing is done using DXA/OVITO. Under changing temperature and stress, the following variations of thermally-activated glide are found: nucleation and expansion of double kinks, formation and recombination of  $1/6\langle 112 \rangle$  Shockley partials, self-pinning and production of debris, formation of sessile  $1/3\langle 111 \rangle$  Frank loops. Velocity function of  $1/2\langle 110 \rangle\{110\}$  dislocations calculated at temperatures  $T = 500\text{--}2000$  K and shear stresses  $\sigma = 10\text{--}1000$  MPa shows a weak temperature dependence and becomes higher than the velocity of  $1/2\langle 110 \rangle\{001\}$  edge dislocations at temperatures  $T < 1250$  K.

## 1. Introduction

There currently exists a certain degree of controversy over the plastic behavior of uranium dioxide. Polycrystalline (sintered) near-stoichiometric uranium dioxide ( $\text{UO}_2$ ) is considered to have a high brittle-to-ductile transition temperature  $T_{\text{BDT}}$ . Different studies report  $T_{\text{BDT}}$  in  $\text{UO}_2$  ranging from 1300 to 1900 K (Scott et al., 1959; Canon et al., 1971; Evans and Davidge, 1969; Baranov et al., 2013; Iltis et al., 2015; Soulacroix et al., 2014). On the other hand, it was shown in compression experiments of  $\text{UO}_2$  single crystals that considerable plastic deformation up to a shear strain  $\varepsilon \approx 1\%$  can be achieved for compressive stresses  $\sigma = 60\text{--}120$  MPa and test temperatures  $T = 523\text{--}873$  K (Keller et al., 1988b). The typical strain rates in these experiments were  $\dot{\varepsilon} = 1 \times 10^{-6} - 5 \times 10^{-4} \text{ s}^{-1}$ , which implies that low-temperature plastic deformation in  $\text{UO}_2$  occurs slowly. These conditions are common to several technological processes, e.g. hot pressing. Therefore, knowledge of low-temperature plasticity might provide ways of improving the fabrication procedure of oxide fuel pellets. In a related case study where  $\text{UO}_{2.06}$  powder was subjected to hot pressing (temperatures  $T = 673\text{--}873$  K, axial compaction stress  $\sigma \leq 95$  MPa, compaction time  $t = 10\text{--}60$  min) several evidences of plastic deformation (or, perhaps, dislocation-

\* Corresponding author. United Kingdom Atomic Energy Authority (UKAEA), Culham Science Centre, Abingdon, Oxfordshire, OX14 3DB, United Kingdom.

E-mail address: [artem.lunev@ukaea.uk](mailto:artem.lunev@ukaea.uk) (A.V. Lunev).

<https://doi.org/10.1016/j.ijplas.2018.07.003>

Received 14 March 2018; Received in revised form 3 July 2018; Accepted 4 July 2018

Available online 21 July 2018

0749-6419/ © 2018 Elsevier Ltd. All rights reserved.

mediated creep) were found by X-ray diffraction: a gradual increase in dislocation density calculated using the Warren-Averbach technique; and texture evolution with compression time manifesting in the displacement of peak pole density on inverse pole figures (IPF) towards {001} symmetrically to the  $\langle 110 \rangle$  directions (Lunev et al., 2017b).

A study by Keller et al. (1988b) reported mostly  $1/2\langle 110 \rangle\{111\}$  slip traces of screw dislocations after deformation of pre-strained uranium dioxide at temperatures  $T = 523\text{--}873$  K. Hence, they suggested that the primary slip system at low temperatures in  $\text{UO}_2$  is  $\langle 110 \rangle\{111\}$  – in contrast to the case of high temperatures, at which the primary slip system was found to be  $\langle 110 \rangle\{001\}$  (Keller et al., 1988a). Other authors are less conclusive on the low-temperature deformation in  $\text{UO}_{2+x}$ . For instance, Alamo et al. (1978) considered the role of  $\{111\}$  slip planes only as auxiliary at temperatures  $T = 973\text{--}1673$  K. Yust and McHargue (1969) pointed out that slip at  $T > 1073$  K on  $\langle 110 \rangle\{110\}$  is also possible. To summarize, only one experimental study has been published so far with information about plastic deformation in  $\text{UO}_{2+x}$  at temperatures  $T < 900$  K.

Data on active slip systems and dislocation mobilities can also be obtained via atomistic modeling, e.g. as it was done recently by (Po et al., 2016; Yanilkin et al., 2014; Cho et al., 2017; Zhou et al., 2016; Gilbert et al., 2011; Tseplyaev et al., 2017). New results on dislocation mobilities for  $\text{UO}_2$  were recently presented by Soulié et al. (2018) in a study using a many-body SMTB-Q potential. They performed dynamic constant-rate deformation tests at  $T = 0$  K and showed that the critical resolved shear stress (CRSS) for glide of screw dislocation was highest on the  $\{110\}$  slip planes and lowest on the  $\{100\}$  slip planes. This is in contradiction with data presented by Skelton and Walker (2017) who showed that for different interatomic potentials based on rigid-ion models, the  $1/2\langle 110 \rangle\{110\}$  edge and screw dislocations are characterized by the highest Peierls stresses, and the minimum Peierls stress for screw dislocation is achieved on  $\{111\}$  slip planes. In contrast, a general consensus has been reached over the fact that  $\{001\}$  is the primary slip plane for edge dislocations (Skelton and Walker, 2017; Parfitt et al., 2010; Fossati et al., 2013), while the  $1/2\langle 110 \rangle\{110\}$  screw dislocations exhibit the lowest line energies (Murphy et al. (2014).

If Peierls barriers are high, the motion of dislocations is thermally activated and usually proceeds by ejection and expansions of double kinks. Interestingly, there is no direct relation between the value of Peierls barrier and the characteristics of kinks observed at high temperatures, such as size, shape, and width. For instance, Rodney and Proville (2009) report a stress dependence of the Peierls potential, which influences the kink pair formation and interaction. For edge dislocation in  $\text{UO}_2$  at high temperatures, there is a variation in thermally-activated regimes of motion depending on stress and temperature (Lunev et al., 2017a). The motion of dislocation lines can be extremely complex, and standard analytical models might fail to describe the dependence of dislocation velocity on stress and temperature.

Since no data is currently available on the mobility of screw dislocations in  $\text{UO}_2$ , it is impossible to conduct complex three-dimensional dislocation dynamics simulations for this material, which require specifying the mobility functions both of edge and screw dislocations (Srivastava et al., 2013; Wang and Beyerlein, 2011; Naamane et al., 2010). This study serves two main purposes: to check whether the supposedly least mobile  $1/2\langle 110 \rangle\{110\}$  screw dislocations are indeed as slow compared to the edge dislocations on the primary slip system in  $\text{UO}_2$ ; and to extract the temperature and stress dependence of their glide velocity, which may be helpful to the development of a dislocation dynamics code.

## 2. Methodology

We used LAMMPS simulation package (Plimpton, 1995) which implements the basic molecular dynamics algorithms optimized for machines supporting message-passing interface (MPI). Dump files generated by LAMMPS were subsequently processed with OVITO software (Stukowski, 2010). The latter used the dislocation extraction algorithm (DXA) developed by Stukowski et al. (2012) to visualize dislocation lines and determine their Burgers vectors. Only uranium atomic positions of the FCC cation sub-lattice were used in OVITO DXA to identify dislocations. Details of the simulation procedure are given below.

### 2.1. Interatomic potential

It was shown in a recent paper (Lunev et al., 2017a) that MOX-07 (Potashnikov et al., 2011) and Morelon (Morelon et al., 2003) potentials are probably the best available semi-empirical potentials for performing simulation of dislocation motion. Because they are designed based on a relatively simple ionic model, these potentials have strong limitations. They do not allow charge variation of individual ions near the dislocation core, which could be modeled by many-body variable charge potentials – e.g. SMTB-Q or COMB Soulié et al. (2018); Sattonnay and Tetot (2013); Li et al. (2013). However, these latter potentials are still in development. Currently, bulk properties of  $\text{UO}_2$  (e.g., lattice parameter, which determines the spacing between adjacent Peierls valleys) are better reproduced using the MOX-07 potential. Another limitation of pair potentials is the impossibility to reproduce the correct relation between elastic constants  $C_{12}$  and  $C_{44}$  – the Cauchy inequality  $C_{12} \neq C_{44}$ . Interestingly, it was shown (Lunev et al., 2017a; Murphy et al., 2014; Skelton and Walker, 2017) that a many-body EAM potential specifically designed to reproduce elastic constants of  $\text{UO}_2$ , but otherwise fully based on Yakub pair potential (Yakub et al., 2009), gives virtually identical results for the core structure, line energies, and glide velocity in  $\text{UO}_2$ . On the other hand, MOX-07 potential also shows good results on surface properties while closely reproducing Pauling's empirical relation for electronegativities. The latter is a strong advantage because Coulombic interaction was found to be one of the major factors influencing dislocation mobility. Previous tests showed that MOX-07 and Morelon (Morelon et al., 2003) potentials displayed very good agreement on the stress dependence of glide velocity of edge dislocations at  $T = 2000$  K (Lunev et al., 2017a), and on the line energies and core structures of edge and screw dislocations (Murphy et al., 2014). Morelon potential was recently used by Chartier et al. (2016) to study nucleation of dislocations in  $\text{UO}_2$  due to radiation damage and is considered trustworthy. For consistency with previous work, the mobility of screw dislocations was studied with the MOX-07 potential.

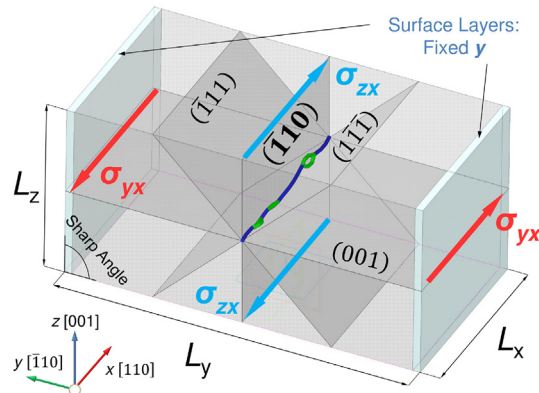


**Fig. 1.** Scheme showing the simulation cell with a  $1/2[110](\bar{1}10)$  screw dislocation line. The dimensions  $L_x$ ,  $L_y$ ,  $L_z$ , and  $xz$  are adjusted to ensure that all components of the stress tensor are zero:  $\langle \sigma_{ik} \rangle_i \approx 0$ . Boundary conditions for the  $x$  and  $z$  axes are periodic, but fixed for the  $y$  axis. Atoms in the buffer layers near  $y = +L_y/2$  and  $y = -L_y/2$  boundaries are kept from moving along the  $y$  axis ( $v_y^i = 0$  for each  $i$ -th atom). The applied shear stress  $\sigma_{yx}$  triggers the dislocation motion on the  $(\bar{1}10)$  crystallographic plane. Other possibilities of whether the parasitic shear stress  $\sigma_{zx}$  is capable of triggering additional motion on either  $(100)$ ,  $(\bar{1}11)$  or  $(1\bar{1}\bar{1})$  planes are considered.

## 2.2. Simulation setup

To simulate dislocation motion, we used the same basic simulation parameters as previously (Lunev et al., 2017a) with a few notable exceptions. Instead of making an orthogonal simulation cell, we introduced a triclinic one characterized by the dimensions  $L_x$ ,  $L_y$ , and  $L_z$  and tilt factors (amounts of displacement applied to the respective faces of an originally orthogonal box)  $xy$ ,  $xz$ , and  $yz$  (Fig. 1). When using this approach, the simulation cell is fully defined by its origin  $\mathbf{O} = (-L_x/2 \ -L_y/2 \ -L_z/2)$  and three edge vectors:  $\mathbf{a} = (L_x + \delta x \ 0 \ 0)$ ,  $\mathbf{b} = (xy \ L_y \ 0)$ , and  $\mathbf{c} = (xz \ yz \ L_z)$ , where  $\delta x$  is a small additional term added to comply with the translational symmetry (e.g. for an FCC lattice  $\delta x = 0.25 \cdot a_0$ , where  $a_0$  is the lattice parameter). The initial values for the  $xy$ ,  $xz$ , and  $yz$  dimensions were zero.

Uranium and oxygen atoms were placed at the nodes of a perfect fluorite crystal structure with a non-relaxed lattice parameter  $a_0 = 0.54695$  nm. The dislocation line was introduced parallel to the  $x$  axis in the center of the simulation cell (Fig. 1) by displacing the atoms from their equilibrium positions according to the expression for the displacement field  $u$  of a single screw dislocation in an elastically isotropic medium. The latter may be derived from the classical theory of elasticity (Anderson et al., 2017):  $u_x = b/(2\pi) \cdot \text{atan}(y - y_0)/z$ ,  $u_y = 0$ ,  $u_z = 0$ , where  $u_j$  is the  $j$ -th component of the displacement vector, and the displacement  $y_0$  is introduced to compensate the  $y$ -drift of the dislocation line during stress relaxation. Boundary conditions were periodic for both  $x$  and  $z$  axes – and fixed for the  $y$  axis. Fixed  $y$  boundaries were set by manually assigning a zero velocity component  $v_y^i = 0$  to each  $i$ -th atom in the respective boundary layers before running the molecular dynamics simulation. A conjugate gradients energy minimization routine was run to adjust the atomic positions due to the presence of a dislocation in the anisotropic crystal. Atoms contained in the  $y$  boundary layers were excluded from the minimization routine to avoid surface distortion. The crystal configurations corresponding to the potential energy minima showed non-zero normal stresses (this was discussed earlier in (Lunev et al., 2017a)), and also a non-zero shear stress component  $\sigma_{zx} \neq 0$ . The latter is due to the superposition of elastic fields create by the screw dislocation and the flat surfaces on  $y$  boundaries. If the latter were not fixed, then energy minimization would result in two dislocations appearing in the simulation cell. However, because only one dislocation was introduced, its strain field induced  $\sigma_{zx} \neq 0$  in an orthogonal simulation cell. The  $\sigma_{zx}$  stress could then be quantified by assuming that the dislocation interacts with its images (or arrays of images) in the vacuum layers adjacent to the  $y = +L_y/2$  and  $y = -L_y/2$  boundaries, e.g. as it was done by Kamat et al. (1987). To zero out the normal stresses  $\sigma_{xx}$ ,  $\sigma_{yy}$ , and  $\sigma_{zz}$  and the shear stress  $\sigma_{zx}$ , an additional relaxation procedure was performed in NVT ensemble by making a series of 50 short 1 ps runs with scaling of the  $L_x$ ,  $L_y$ ,  $L_z$ , and  $xz$  dimensions following each run. This iterative procedure resulted in the simulation cell changing four of its dimensions (and respective components of the stress tensor) and reaching  $xz \approx 0.170 - 0.192$  nm for different  $L_x$ ,  $L_y$ , and  $L_z$  values.

An additional force  $f_z(t) = \sigma_{yx}(t)L_xL_z/N_k$  creating  $xy$  shear was applied to each of the  $N_k$  ( $k = +y, -y$ ) atoms contained in the  $y$ -boundary layers (Fig. 1). The piecewise function  $\sigma_{yx}(t)$  was defined in the following way: a linear ramp  $\sigma_{yx}(t) = \sigma \cdot (t/t_0)$ , where  $t_0 = 20$  ps and  $\sigma$  is a constant value, at  $t = 0-20$  ps; and  $\sigma_{yx}(t) = \sigma$  at  $t > 20$  ps. Glide was expected to occur parallel to the  $z$  axis on the  $(\bar{1}10)$  crystallographic plane.

## 3. Results and discussion

Simulation of dislocation glide was performed at temperatures  $T = 500-2000$  K (step  $\Delta T = 250$  K) and in the range of shear stresses  $\sigma = 10-1000$  MPa. The following range of simulation times could be achieved with the available computing power:  $t = 0.5-2.0$  ns. Longer runs were required at low stresses and temperatures when the dislocation moved in discrete steps, the time interval between them becoming comparable to the total duration of simulation.

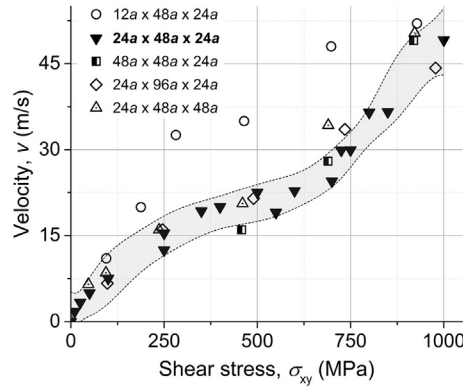


**Fig. 2.** The influence of simulation cell dimensions on the glide velocity of  $1/2\langle 110 \rangle$  screw dislocation in  $\text{UO}_2$  at  $T = 2000$  K. For sufficiently large simulation cells, the simulation data is confined to a narrow region of the plot (marked in gray), which suggests that converging results are obtained.

### 3.1. Preliminary tests

#### 3.1.1. Dimensions of the simulation box

First tests were carried out to explore the simulation conditions at which converging values for the dislocation glide velocity  $v(\sigma, T)$  could be obtained. This task narrows down to choosing the proper simulation cell dimensions:  $L_x$  (length of the dislocation line),  $L_y$  (distance between fixed boundary surfaces), and  $L_z$  (length of glide path). All tests were done at a temperature  $T = 2000$  K, which is the highest considered in this work. The following  $L_x \times L_y \times L_z$  configurations of the simulation cells were considered:  $12a \times 48a \times 24a$ ,  $24a \times 48a \times 24a$ ,  $48a \times 48a \times 24a$ ,  $24a \times 96a \times 24a$ , and  $24a \times 48a \times 48a$  where  $a = a(T)$  is the equilibrium crystal structure parameter of  $\text{UO}_2$  at a temperature  $T$ .

Test results (Fig. 2) show that very small dislocation lines ( $l = L_x = 12a$ ) introduce significant error resulting in overestimation of dislocation velocity  $v(\sigma)$  at  $T = 2000$  K. As discussed by Gilbert et al. (2011), this is mainly because smooth dislocation motion via propagation of kinks on the glide plane is easier when the formation of cross-kinks on orthogonal planes is suppressed. Gilbert et al. (2011) suggested that using shorter dislocation lines, which allow for the formation only of a single kink pair, is preferable. However, because one of the intermediate goals in this work was to establish the modes of thermally activated motion, we considered relatively large values of the  $L_x$  dimension. It was expected that the motion of individual kink pairs does not change when increasing simulation box dimensions. As seen in Fig. 2, for sufficiently large simulation cells dislocation velocity is size-independent.

The following dimensions of the simulation cell were selected for dislocation velocity calculation:  $24a \times 48a \times 24a$  (330,480 atoms). For a detailed analysis at high stresses, large simulation cells ( $48a \times 48a \times 24a$ ) were used because of strong bending of dislocations lines.

#### 3.1.2. Active slip systems

For all configurations considered here, a  $v_y \neq 0$  component of dislocation velocity appeared due to the non-zero parasitic shear stress:  $\sigma_{xz}(t) \neq 0$  (Fig. 3). The  $y$ -drift caused by the latter would lead to the dislocation eventually reaching the respective surface, which limited the maximum simulation time available for evaluation of the dislocation velocity  $v_z$  (and hence the larger random error). Interestingly,  $y$ -drift paused every time when  $\sigma_{xz}$  reached a plateau (Fig. 3a). The maximum value of  $\sigma_{xz}$  was found to depend on the simulation box dimensions and the simulation temperature  $T$  (e.g., at  $T = 2000$  K:  $\sigma_{xz} \leq 20 - 30$  MPa for cells with  $L_x = 24a$ ,  $L_y = 96a$  and  $L_z = 24a$ ,  $\sigma_{xz} \leq 15 - 20$  MPa for cells with  $L_x = 24a$ ,  $L_y = 48a$  and  $L_z = 48a$ ,  $\sigma_{xz} \leq 120$  MPa for  $L_x = 24a$ ,  $L_y = 48a$  and  $L_z = 24a$ ). Typically, the ratio between the components of the dislocation velocity was  $|v_y/v_z| \approx 0.05-0.3$  and was found to decrease with temperature  $T$  and  $\sigma_{xy}$  stress. However, at  $T = 500-750$  K this ratio was greater than unity, i.e.  $y$ -motion was faster than the  $z$ -motion.

Because of the  $v_y \neq 0$  component, the dislocation could be experiencing complex motion on the following crystallographic planes: (a) either  $(\bar{1}11)$  or  $(\bar{1}\bar{1}\bar{1})$ ; (b) both  $(\bar{1}10)$  and  $(001)$ ; (c) a combination of the above. The resolved shear stress  $\tau_s$  for the slip system  $s$  is given by:  $\tau_s = \sigma_{ij}n_i m_j$ , where  $\sigma_{ij}$  is the stress tensor,  $n_i$  is the  $i$ -th component of the slip plane normal,  $m_j$  is the  $j$ -th component of the slip direction ( $m_j = b_j/b$ ). The  $\tau_s$  values calculated for the slip planes above are:  $\tau_{(\bar{1}10)} = \sigma_{xy}$ ,  $\tau_{(\bar{1}\bar{1}\bar{1})} = \frac{1}{\sqrt{2}}(\sigma_{xy} + \sigma_{xz})$ ,  $\tau_{(\bar{1}\bar{1}\bar{1})} = \frac{1}{\sqrt{2}}(\sigma_{xy} - \sigma_{xz})$ ,  $\tau_{(001)} = \sigma_{xz}$ . In this case,  $v_y(\sigma_{xy}, \sigma_{xz}) = v_{(\bar{1}\bar{1}\bar{1})}(\sigma_{xz} + \sigma_{xy}) + v_{(001)}(\sigma_{xz})$  (here round brackets denote functional dependence). When  $\sigma_{xz} = 0$  and, consequently,  $v_s(\sigma_{xz}) \equiv 0$  – it follows that  $v_y(\sigma_{xy}) = v_{(\bar{1}\bar{1}\bar{1})}(\sigma_{xy})$ . Hence, if the dislocation motion on the  $(\bar{1}11)$  slip system is possible for the geometry described above and if  $\sigma_{xy}(t) = \text{const}$ , at any moment of time there will be a non-zero  $v_y(t) = \text{const}$  velocity component. However, quite the opposite was found during simulation, since no significant correlation was found between  $y(t)$  and  $\sigma_{xy}$  (Fig. 3). Bearing the above arguments in mind, it follows that the dislocation trajectory could only be produced by a superposition of displacements on orthogonal  $(001)$  and  $(\bar{1}10)$  planes. This means that  $v_z = v_{\{\bar{1}10\}}$ , which is used later to calculate the dislocation velocity on the  $(\bar{1}10)$  slip plane. Here and below the following notations are used:  $v := v_z$ ,  $\sigma := \sigma_{xy}$ .

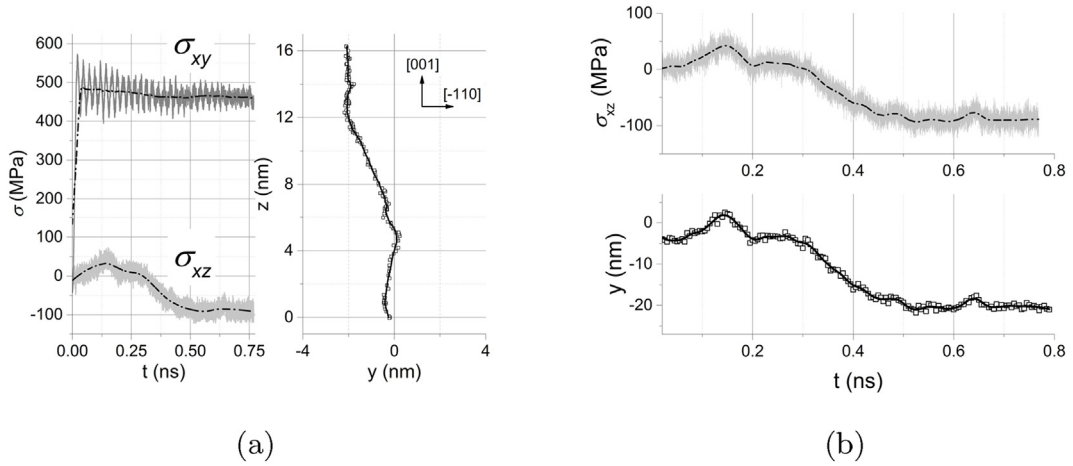


**Fig. 3.** Graphs showing the influence of  $\sigma_{xy}$  and  $\sigma_{xz}$  shear stresses on the trajectory of dislocation's center-of-mass at  $T = 2000$  K,  $\sigma_{xy} \approx 500$  MPa: (a) The time dependence of shear stresses  $\sigma_{xz}(t)$  and  $\sigma_{xy}(t)$ , and the trajectory in  $y$ - $z$  coordinates; (b) correlation between the  $y(t)$ -component of the trajectory and  $\sigma_{xz}(t)$ . Stress oscillates both due to the thermal vibrations and the reflection of elastic waves caused by applying fixed forces to atoms on  $y$  boundary layers. These oscillations are eliminated from analysis by applying a smoothing operation (bold lines). The  $\sigma_{xz}(t)$  curves thus obtained show a number of local extrema (an artifact of the simulation setup), which manifest as turning points on the  $y(t)$  component of dislocation trajectory. On the other hand,  $z(t)$  used to calculate  $v_z = v_{\bar{1}10}$  is unaffected by these features. This is proven by the fact that  $\langle v_z \rangle_\tau$  averaged over sufficiently large time intervals  $\tau$  does not change with time  $t$  – if neither does the average  $\langle \sigma_{xy} \rangle_\tau$ .

### 3.2. Modes of motion

Specific motion mechanisms of the  $1/2\langle 110 \rangle\{110\}$  screw dislocation were analyzed based on the shape of the dislocation line evaluated for each of the stored spatial configurations of atoms discretely registered at equal time intervals for each simulation run. Four modes of dislocation motion (Fig. 4) were identified, each of them activated at different conditions. These are listed below in order of increasing stress and temperature.

#### 3.2.1. Nucleation and expansion of double kinks (Fig. 4a)

Screw dislocations move by ejecting double kinks to the next Peierls valley in their glide direction. If the kink pair is stable, the double kink can then expand, thus resulting in an overall movement of the dislocation on the glide plane. Once it starts expanding, it cannot shrink back. However, only critical-sized double kinks can expand. The expansion of the latter occurs relatively fast compared to their nucleation. Nucleation of critical-sized double kinks, a thermally- and stress-activated process, controls the dislocation velocity;

#### 3.2.2. Self-pinning (Fig. 4b)

Double kinks on the screw dislocation may appear on either of the (001), ( $\bar{1}10$ ) or  $\{111\}$  slip planes. At low  $\sigma$  and  $T$ , when the formation rate of double kinks on the ( $\bar{1}10$ ) plane is small, all meta-stable kinks on the (001) and  $\{111\}$  planes have sufficient time to annihilate. It was noticed that kinks on the (001) plane nucleated more frequently than on the  $\{111\}$  or  $\{110\}$  slip planes – apparently due to the different formation energies. However, at  $\sigma > \sigma_{S-P}(T)$ , where  $\sigma_{S-P}(T)$  is a threshold stress, the dislocation line forms ( $\bar{1}10$ ) kinks much quicker than on any other plane. It is typical at these conditions that the dislocation line, most of which has progressed towards the [001] direction on the ( $\bar{1}10$ ) plane, becomes entangled by the (001) double kink left behind (i.e., stretched across the ( $\bar{1}11$ ) plane). As suggested by Petukhov (2001), this intrinsic local obstacle acts as a topological limitation for the dislocation motion driven by the ( $\bar{1}10$ ) double kinks. The sequence of events leading to pinning is shown on Fig. 5. Non-uniform motion of the dislocation line is observed with superkinks stretching across several Peierls valleys on the ( $\bar{1}10$ ) plane. When the dislocation line is stretched to its limit, it is held by the pinned segments.

To characterize the self-pinning process, the quantity  $t_{pin}(\sigma, T)$  is introduced – the average time spent by a dislocation segment in the pinned state at a given temperature  $T$  and shear stress  $\sigma_{xy}$ . This characteristic time was determined from MD data (Fig. 6). It was observed that  $t_{pin}$  increases with  $T$  and  $\sigma_{xy}$  at  $\sigma \lesssim 800$  MPa, meaning that a single mechanism controls unpinning at these stresses. Since the latter process is clearly thermally-activated, it may be described with the following equation (see e.g. (Blum, 2018)):

$$t_{pin} = t_0 \cdot \exp\left(-\frac{E_0 - V_0 \sigma}{kT}\right), \quad (1)$$

where  $t_0$ ,  $E_0$  (activation energy), and  $V_0$  (activation volume) are model parameters. Eq. (1) reflects the fact that stress increases the stability of cross-kinks on adjacent slip planes. The parameters were found from fitting to MD data:  $t_0 = (5.24 \pm 3.12)$  ns,  $E_0 = (1.02 \pm 0.17)$  eV, and  $V_0 = (0.140 \pm 0.025)$  nm<sup>3</sup>, which is equivalent to  $V_0 \approx 2.5b^3$ . Analytical curves calculated with Eq. (1) are shown on Fig. 6 alongside MD data. At  $\sigma > 800$  MPa the dependence of  $t_{pin}$  on  $\sigma$  and  $T$  is more complex, apparently with more than

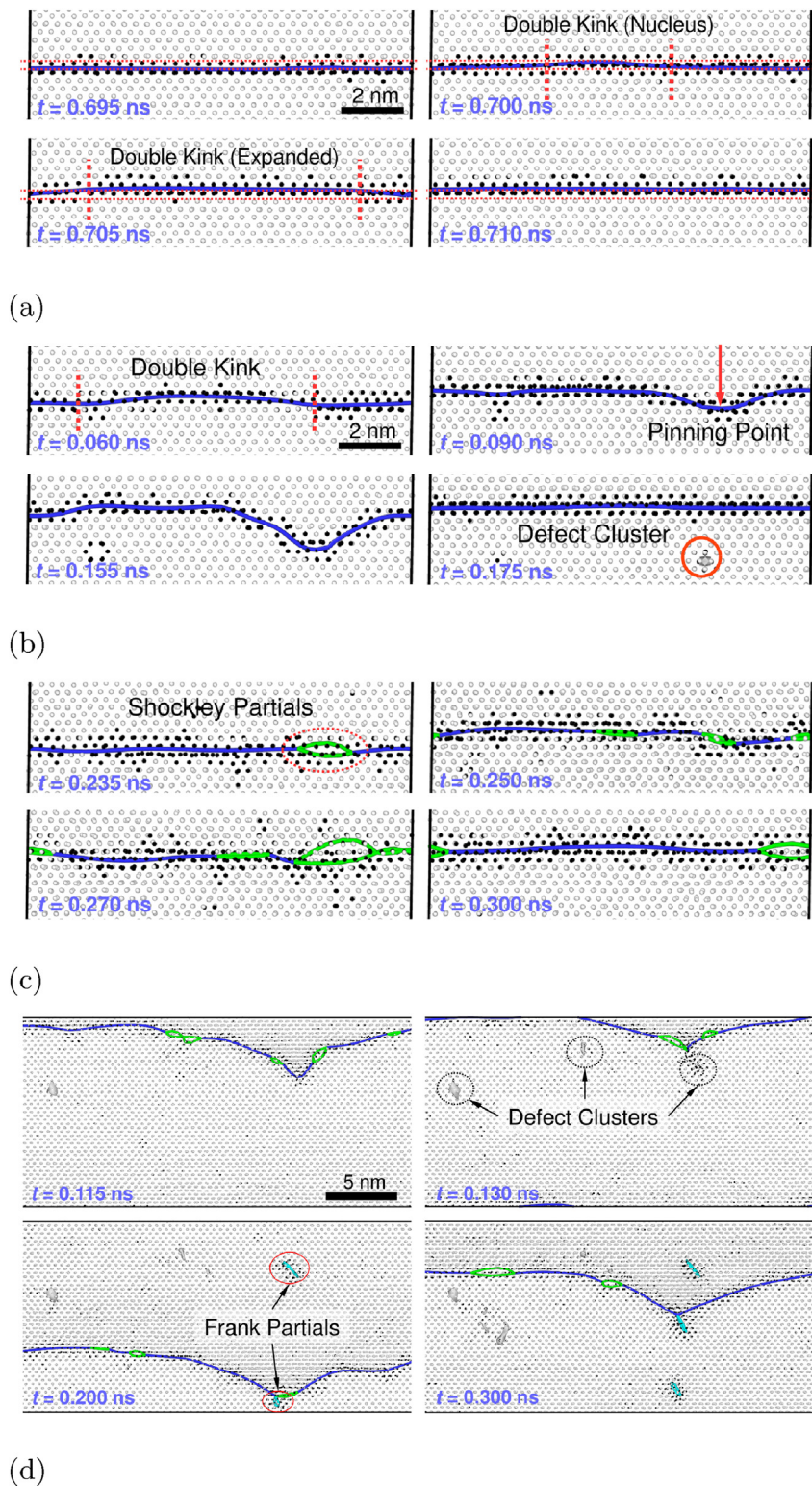


**Fig. 4.** The different modes of thermally activated motion of the  $1/2[110](\bar{1}10)$  screw dislocation in  $UO_2$  as observed in simulations at the following characteristic conditions: (a)  $T = 1000$  K,  $\sigma = 600$  MPa; (b)  $T = 1000$  K,  $\sigma = 1000$  MPa (the pinning points appear where cross-kinks are formed on adjacent crystallographic planes); (c)  $T = 2000$  K,  $\sigma = 100$  MPa; (d)  $T = 2000$  K,  $\sigma = 1000$  MPa (note a defect cluster left behind the dislocation line later becomes identified as a Frank loop). The field of view was moving with the dislocation on (a)–(c).

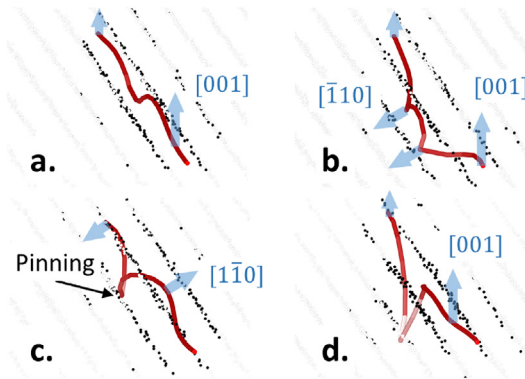


**Fig. 5.** The sequence of events leading to self-pinning of a  $1/2[110](\bar{1}10)$  screw dislocation ( $T = 1000$  K,  $\sigma = 1000$  MPa): (a) The dislocation moves by ejecting double kinks on the  $(\bar{1}10)$  crystallographic plane due to the  $\sigma_{xy}$  applied shear stress; (b) Meta-stable double kinks are formed on the  $(001)$  plane; (c) A knot (topological defect) is formed on the dislocation line; (d) The knot causes pinning and formation of superkinks. Color indicates the local character: red – screw segments, white – mixed segments. The field of view is moving with the dislocation. (For interpretation of the references to colour in this figure legend, the reader is referred to the Web version of this article.)

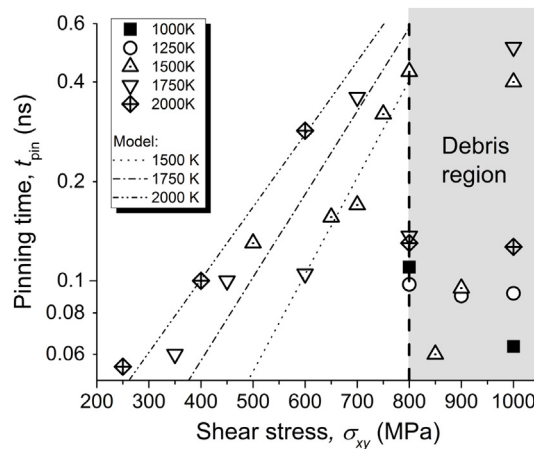


**Fig. 6.** Evolution of the self-pinning time  $t_{\text{pin}}$  with temperature  $T$  and shear stress  $\sigma_{xy}$  for the  $1/2(110)$  screw dislocation in  $\text{UO}_2$ : molecular dynamics data (points) and curves obtained with Eq. (1) (lines). A dislocation segment  $i$  ( $i = 1, 2, \dots, N$ ) is considered to be pinned at time  $t$  if its velocity  $v_i(t)$  is much lower than the average dislocation velocity  $\langle v_i \rangle(t)$ .

one unpinning process taking place.

To summarize, during self-pinning the dislocation experiences a sequence of transitions between *meta-stable* locked states, e.g. with sessile cross-kinks, and *stable* glissile state. This is opposite to the case considered by Caillard et al. (1993), where the glissile state is *meta-stable*. In the latter model, line tension drives the pinned segments back to the glide plane. In this work, the pinning time is governed by the probability of the transition to the meta-stable state, which may increase with temperature  $T$  and stress  $\sigma$ . On a side note, self-pinning by cross-kinks was first observed in atomistic simulations by Marian et al. (2004). Interestingly, superkinks were also found on  $1/2\langle 110 \rangle\{001\}$  edge dislocations in  $\text{UO}_2$  earlier (Lunev et al., 2017a). However, for the latter case the dislocation line could not stretch out of the glide plane and there was no apparent pinning. For screw dislocations the probability of forming cross-kinks in several directions is non-zero, and hence self-pinning results from the complex non-planar motion of a screw dislocation;

### 3.2.3. Core splitting out of the glide plane (Fig. 4c)

In some FCC metals, as shown in atomistic simulation by Rao et al. (2015), individual segments of a screw dislocation may dissociate into Shockley partials separated at short distances. This partial dissociation process is possible due to the modification of the dislocation core also known as the formation of constrictions. Constrictions allow the otherwise planar dislocation core to locally expand on the adjacent cross-slip plane (the Friedel-Escaig model, see e.g. Caillard and Martin (1989)). During this process, a stacking fault is formed, which is enclosed between two partials. For  $\text{UO}_2$ , thermally-activated nucleation of  $1/6\langle 112 \rangle$  Shockley partials was observed. Most of the time the dislocation line stays in a ground (non-dissociated) state with occasional partial dissociation events (which may be regarded as transitions to excited states). The configuration on Fig. 4c shows that the following dissociation reactions take place:  $1/2[\bar{1}\bar{1}0] = 1/6[\bar{2}\bar{1}\bar{1}] + 1/6[\bar{1}\bar{2}\bar{1}]$  and  $1/2[\bar{1}\bar{1}0] = 1/6[\bar{1}\bar{2}\bar{1}] + 1/6[\bar{2}\bar{1}\bar{1}]$ . A similar reaction has been analyzed for  $\text{UO}_2$  by Fossati et al. (2013), and it was shown to be energetically favorable (at least for the Morelon potential). However, it was suggested by

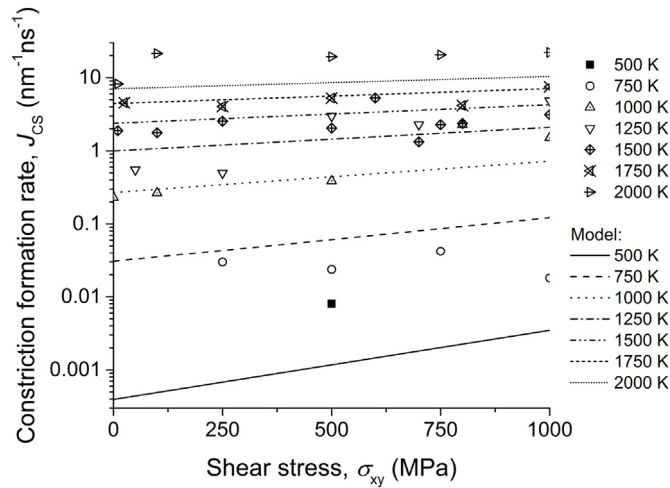


Fig. 7. Evolution of the constriction formation rate  $J_{CS}$  with temperature  $T$  and shear stress  $\sigma_{xy}$  for the  $1/2[110](\bar{1}10)$  screw dislocation in  $UO_2$ : molecular dynamics data (points) and curves obtained with Eq. (2) (lines). The rate  $J_{CS}$  has been evaluated from MD data by counting the number of dissociated segments over a period of simulation time and divided by the length of the screw dislocation  $l = L_x$ .

Skelton and Walker (2017) that dissociation is unlikely to take place due to extremely narrow core of a  $1/2\langle 110 \rangle \{110\}$  screw dislocation. Because splitting of the dislocation core happens on the  $\{111\}$  atomic planes, the analysis conducted by Skelton and Walker (2017) using the Peierls-Nabarro model seems to be invalidated for this dislocation type. As shown by Fossati et al. (2013) for the Morelon potential, the maximum spacing (i.e., widening of the dislocation core) between the  $1/6\langle 112 \rangle$  partials is  $d_p \approx 2b$ . Roughly the same sizes of the stacking faults are seen in current simulation.

The intrinsic stacking faults on the  $\{111\}$  (cross-slip) planes enclosed between the Shockley partials have a very high energy  $f = 0.96 \text{ J/m}^2$  (data reported by Fossati et al. (2013)). Hence the very short life-times of the excited states. Despite this, the constriction formation rate  $J_{CS}$  increases with temperature and stress (Fig. 7). The Gibbs free energy of a single constriction in Escaig's model is written as (Caillard and Martin, 1989):  $\Delta G_{CS} = 2\mu\tilde{A}D_0^2f[(1 - b_0/D_0)^2 - \alpha\tilde{\tau}b/f]$ , where  $D_0$  is the dissociation width at zero stress,  $b_0$  is the width of a recombined dislocation,  $\mu$  is the shear modulus,  $\alpha$  is an orientation-dependent parameter,  $\tilde{A}$  is a slowly variable function of  $\mu$ ,  $b$ , and  $f$ , and  $\tilde{\tau} \approx \sigma_{xy}$  is the shear stress. This can be rewritten as  $\Delta G_{CS} = \mu(T)/\mu(T_0) \cdot (E_1 - V_1\tilde{\tau})$ , where  $E_1$  and  $V_1$  are constants. The constriction formation rate may then be described using an equation similar to Eq. (1):

$$J_{CS} = J_0 \cdot \exp\left(-\frac{1}{kT} \left[ \frac{\mu(T)}{\mu(T_0)} (E_1 - V_1\tilde{\tau}) \right]\right), \quad (2)$$

where the parameters  $J_0 = (58 \pm 17) \text{ nm}^{-1} \text{ ns}^{-1}$ ,  $E_1 = (0.56 \pm 0.05) \text{ eV}$ ,  $V_1 = 0.016 \pm 0.008 \text{ nm}^3$  (this corresponds to  $f = 0.96 \text{ J/m}^2$  and  $\alpha = 0.14$ ) have been obtained by fitting to the data presented on Fig. 7, and data on the shear modulus dependence on temperature  $\mu(T)$  has been taken from Marlowe (1969).

In this simulation, it was not possible to detect significant cross-slip on the  $\{111\}$  planes induced by the  $1/6\langle 112 \rangle$  partials. Instead, it is suggested that the Shockley partials, which combine both screw and edge segments, create additional intrinsic local obstacles for dislocation glide on the  $\{110\}$  planes. This is somewhat similar to the locking-unlocking mechanisms discussed by Caillard and Martin (1989).

### 3.2.4. Production of defect clusters and ejection of Frank loops (Fig. 4d)

After unpinning, especially at a high applied stress, nucleation of point defect clusters is often observed (Fig. 4b). Although the latter might play the role of extrinsic obstacles when encountered by a dislocation, they are short-lived. When these clusters are formed, unpinning seems to occur more rapidly (Fig. 8). At very high temperatures and stresses, unpinning occurs with the ejection of either  $1/3[111]$  or  $1/3[11\bar{1}]$  Frank loops next to the pinning points. These loops are considerably more stable than the Shockley partials and are sessile. Hence, if they interact with the dislocation line, they can present additional obstacles to its motion. The stretching limit for the dislocation line, i.e. the maximum height of the superkinks, seems to increase when Frank loops can be ejected (e.g. compare 4b and 4d). Interestingly, if a Frank loop forms next to two Shockley partials, they become connected by a  $1/6\langle 110 \rangle$  stair-rod dislocation. At high temperatures and stresses (e.g. at  $T = 2000 \text{ K}$  and  $\sigma = 1000 \text{ MPa}$ )  $1/3\langle 001 \rangle$  Hirth dislocations connecting neighboring Shockley partials were also observed. This is similar to the overlap of partials shown by Granberg et al. (2017) for Fe-Cr alloys. Formation of Frank loops occurs more easily in case of longer dislocation lines ( $L_x = 48a$ ).

To summarize the observations above, a map has been drawn to show the distinct regions in which a  $1/2\langle 110 \rangle$  screw dislocation moves according to different mechanisms (Fig. 8). It may be seen that even in the simplest case when the dislocation does not experience any self-pinning or formation of Frank partials and defect clusters, the probability of core splitting is still significant.

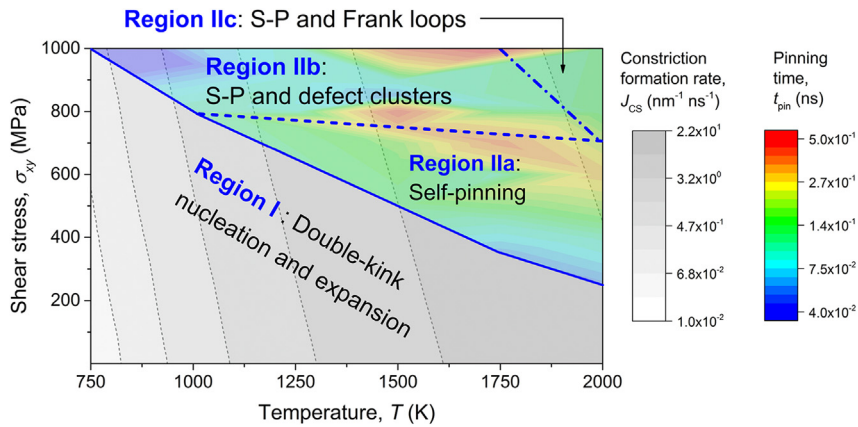


Fig. 8. A map in  $T - \sigma_{xy}$  coordinates showing the occurrence of different mechanisms of motion for the  $1/2\langle 110 \rangle$  screw dislocation in  $UO_2$  based on analysis conducted with the DXA sequence of images.

### 3.3. Glide velocity function $v_{\{110\}} = v_z(\sigma_{xy}, T)$

The dislocation velocity data extracted from MD simulations at different temperatures is shown in Fig. 9. Because the motion of  $1/2\langle 110 \rangle\{110\}$  screw dislocations is complex and involves many sub-processes and features as discussed in Sect. 3.2, there is no simple functional form that can describe all data obtained in this work. However, the collected data shows noteworthy trends:

- Although the motion of screw dislocations is thermally activated (as discussed in Sect. 3.2), the temperature dependence of their

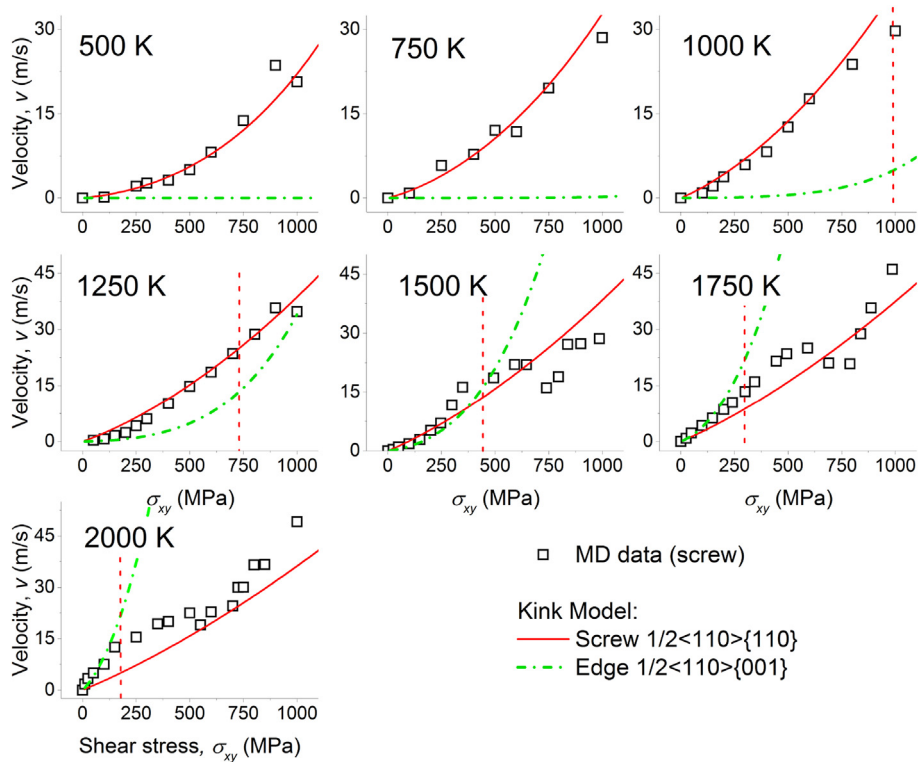


Fig. 9. Glide velocity of the  $1/2\langle 110 \rangle$  screw dislocation in  $UO_2$  calculated at  $T = 500\text{--}2000$  K and  $\sigma = 10\text{--}1000$  MPa. Dotted vertical lines represent the critical stress at which self-pinning of dislocation segments happens and thus marks the applicability limit of the kink model (the position of these lines also roughly coincides with the first inflection points on the respective curves). The red solid line is plotted using dislocation velocity expression with parameters from Table 1. Green dash-dotted line corresponds to the same expression, but with a different set of parameters previously obtained for the  $1/2\langle 110 \rangle\{001\}$  edge dislocation (Lunev et al., 2017a). (For interpretation of the references to colour in this figure legend, the reader is referred to the Web version of this article.)

**Table 1**

Fitting parameters for the dislocation velocity expression based on the generalized double-kink nucleation and expansion formalism <sup>a</sup>:  $v = A \cdot \sigma^{3/4} K_1^{-1/2} (B \sqrt{\sigma} / kT) \cdot \exp(-U_0/kT) / \sqrt{kT}$ .

Fitting parameter		Dislocation type and slip plane	
		Screw {110}	Edge {100} <sup>a</sup>
A	(nm <sup>3.25</sup> / eV <sup>1/4</sup> ns)	7.02 ± 0.39	(0.74 ± 0.33) × 10 <sup>3</sup>
B	(eV <sup>1/2</sup> nm <sup>3/2</sup> )	0.096 ± 0.010	0.39 ± 0.03
U <sub>0</sub>	(eV)	0.208 ± 0.013	1.38 ± 0.07

<sup>a</sup> Lunev et al. (2017a).

glide velocity seems to be much weaker than in case of 1/2{110}<001> edge dislocations. At low temperatures ( $T < 1250$  K), screw dislocations are faster. At first, this seems surprising considering they also have the highest Peierls barriers according to the data provided by Skelton and Walker (2017). However, the latter was obtained within the framework of Peierls-Nabarro model, which is known to become increasingly inaccurate for dislocations with narrow cores (Bulatov and Kaxiras, 1997). It was also shown by Skelton and Walker (2017) that 1/2{110}<110> screw dislocations in UO<sub>2</sub> have the narrowest cores compared to other dislocations. Hence, the model which does not account for changes of the dislocation shape during translation is expected to give gross overestimation of the Peierls stress (Bulatov and Kaxiras, 1997);

- At low stresses ( $\sigma = 10 - 300$  MPa) and  $750 \text{ K} \leq T \leq 1250$  K, glide velocity increases slightly when the temperature decreases. This can probably be explained by the increased probability of splitting the dislocation segments into partials at higher temperatures (Fig. 8), and the delays in motion might be caused by a finite time required for recombination;
- At  $T = 1500 - 2000$  K two inflection points, one at moderate stress and one at high stress, are observed on the velocity-stress curve. The first one results in a slower rate at which dislocation velocity increases with stress. This may be attributed to the activation of self-pinning, as discussed in Sect. 3.2. The second one might be attributed to the activation of a more effective unpinning mechanism (formation of Frank loops).

A velocity function employed previously to describe the kink-driven motion of 1/2{110}<001> edge dislocations (Lunev et al., 2017a) has been used to fit molecular dynamics data obtained in this work for the 1/2{110}<110> screw dislocation type. Only part of the data was selected corresponding to temperatures and stresses at which the formation of double kinks was directly observed (Fig. 8). Parameters of the velocity function obtained by fitting are summarized in Table 1. Fig. 9 shows the corresponding velocity-stress curves at  $T = 500 - 1000$  K, which are compared to curves plotted using the same analytical model but with a different set of parameters describing the velocity of 1/2{110}<001> edge dislocations. It is clearly shown that 1/2{110}<110> screw dislocations move much faster than the 1/2{110}<001> edge dislocations at  $T < 1250$  K. This suggests that a change of the primary slip system in UO<sub>2</sub> happens at  $T \approx 1250$  K.

The kink model seems to offer a good approximation of the MD data at  $T \leq 1250$  K. However, the value of  $U_0$  (effective Peierls barrier) presented in Table 1 is surprisingly low. At high temperatures ( $T \geq 1500$  K), the model seems to underestimate the actual velocity obtained with MD simulation. This could have the same reasons as discussed previously in (Lunev et al., 2017a), namely, breakdown of the elastic theory used for calculating the double-kink formation rate and inapplicability of the diffusion equation.

#### 4. Conclusions

The motion of 1/2{110}<110> screw dislocations in UO<sub>2</sub> is influenced by several thermally- and stress-activated processes including: partial dissociation according to the Friedel-Escaig mechanism; processes of pinning and unpinning due to the formation of cross-kinks on adjacent slip planes. Unlike the case of edge dislocations in UO<sub>2</sub>, the motion of which is restricted to the glide plane, screw dislocations may glide on different planes, and their motion is therefore inherently three-dimensional even when trying to restrict it to a single plane. Nucleation and expansion of double kinks serves as the driving force of glide, while other processes act as limiting factors and add complexity, especially at high temperatures.

It is not yet possible to provide a complete analytical description of dislocation glide mobility for the conditions considered here. However, for relatively low temperatures ( $T \leq 1250$  K) where pinning and dissociation events are rare, a model for kink-controlled motion may still be used with good accuracy to describe MD data up to high stresses resulting in a good quality of fit. This may be useful for further meso-scale calculations. Fitting parameter for the equations describing the dependence of pinning time and constriction formation rate on shear stress and temperature presented in this work may be used in future generalized models of dislocation glide.

Surprisingly, the mobility of the 1/2{110}<110> screw dislocations considered in this work is higher at  $T \leq 1250$  K than the mobility of 1/2{110}<001> edge dislocations. The difference in velocity can reach several orders of magnitude at low temperatures. The latter is unexpected because the 1/2{110}<110> screw dislocation were thought to have the highest Peierls barrier (based, however, on a Peierls-Nabarro model which cannot be applied in case of a narrow non-planar dislocation core). This contradiction seems to support our original hypothesis that thermally-activated glide is not governed uniquely by the value of Peierls barrier defined at  $T = 0$  K for a perfectly straight and non-dissociated dislocation.

## Acknowledgements

A.V.L. acknowledges the financial support of the Russian Foundation for Basic Research (personal grant No. 16-38-60016 mol\_a\_dk). Calculations were performed on Lomonosov supercomputer at the Supercomputing Centre of Moscow State University and on MVS-10P cluster at the Interdepartmental Supercomputing Center of the Russian Academy of Sciences. A.V.L. would like to thank Dr. A. Breidi and Dr. M. Boleininger as well as other staff members working at the Materials Science & Scientific Computing department of UKAEA for helpful discussions of simulation results.

## References

- Alamo, A., Lefèbvre, J.M., Souillard, J., 1978. Deformation plastique du bioxyde d'uranium: observation des sous-structures de dislocations. *J. Nucl. Mater.* 75, 145–153. [https://doi.org/10.1016/0022-3115\(78\)90038-7](https://doi.org/10.1016/0022-3115(78)90038-7).
- Anderson, P.M., Hirth, J.P., Lothe, J., 2017. *Theory of Dislocations*. Cambridge University Press.
- Baranov, V., Devyatko, Y., Tenishev, A., Khlunov, A., Khomyakov, O., 2013. Sintering of oxide nuclear fuel: plastic flow mechanism. *J. Nucl. Mater.* 432, 52–56. <https://doi.org/10.1016/j.jnucmat.2012.07.050>.
- Blum, W., 2018. Discussion: activation volumes of plastic deformation of crystals. *Scripta Mater.* 146, 27–30. <https://doi.org/10.1016/j.scriptamat.2017.10.029>.
- Bulatov, V.V., Kaxiras, E., 1997. Semidiscrete variational peierls framework for dislocation core properties. *Phys. Rev. Lett.* 78, 4221–4224. <https://doi.org/10.1103/PhysRevLett.78.4221>.
- Caillard, D., Couret, A., Molenat, G., 1993. Mechanisms of yield stress anomalies in beryllium and Ni<sub>3</sub>Al. In: KOSTORZ, G., CALDERON, H., MARTIN, J. (Eds.), *Fundamental Aspects of Dislocation Interactions*. Elsevier, pp. 69–81. <https://doi.org/10.1016/B978-1-4832-2815-0.50011-5>.
- Caillard, D., Martin, J.L., 1989. Some aspects of cross-slip mechanisms in metals and alloys. *J. Phys. France* 50, 2455–2473. <https://doi.org/10.1051/jphys:0198900500180245500>.
- Canon, R.F., Roberts, J.T.A., Beals, R.J., 1971. Deformation of UO<sub>2</sub> at high temperatures. *J. Am. Ceram. Soc.* 54, 105–112. <https://doi.org/10.1111/j.1151-2916.1971.tb12230.x>.
- Chartier, A., Onofri, C., Brutzel, L.V., Sabathier, C., Dorosh, O., Jagielski, J., 2016. Early stages of irradiation induced dislocations in urania. *Appl. Phys. Lett.* 109, 181902. <https://doi.org/10.1063/1.4967191>.
- Cho, J., Molinari, J.F., Ancaix, G., 2017. Mobility law of dislocations with several character angles and temperatures in fcc aluminum. *Int. J. Plast.* 90, 66–75. <https://doi.org/10.1016/j.ijplas.2016.12.004>.
- Evans, A., Davidge, R., 1969. The strength and fracture of stoichiometric polycrystalline UO<sub>2</sub>. *J. Nucl. Mater.* 33, 249–260. [https://doi.org/10.1016/0022-3115\(69\)90019-1](https://doi.org/10.1016/0022-3115(69)90019-1).
- Fossati, P., Brutzel, L.V., Devincere, B., 2013. Molecular dynamics simulation of dislocations in uranium dioxide. *J. Nucl. Mater.* 443, 359–365. <https://doi.org/10.1016/j.jnucmat.2013.07.059>.
- Gilbert, M.R., Queyreau, S., Marian, J., 2011. Stress and temperature dependence of screw dislocation mobility in  $\alpha$ -Fe by molecular dynamics. *Phys. Rev. B* 84, 174103. <https://doi.org/10.1103/PhysRevB.84.174103>.
- Granberg, F., Byggmatar, J., Sand, A.E., Nordlund, K., 2017. Cascade debris overlap mechanism of  $\langle 100 \rangle$  dislocation loop formation in Fe and FeCr. *EPL (Europhys. Lett.)* 119, 56003. <https://doi.org/10.1209/0295-5075/119/56003>.
- Iltis, X., Gey, N., Cagna, C., Hazotte, A., Sornay, P., 2015. Microstructural evolution of uranium dioxide following compression creep tests: an EBSD and image analysis study. *J. Nucl. Mater.* 456, 426–435. <https://doi.org/10.1016/j.jnucmat.2014.10.005>.
- Kamat, S., Hirth, J., Carnahan, B., 1987. Image forces on screw dislocations in multilayer structures. *Scripta Metall.* 21, 1587–1592. [https://doi.org/10.1016/0036-9748\(87\)90306-1](https://doi.org/10.1016/0036-9748(87)90306-1).
- Keller, R.J., Mitchell, T.E., Heuer, A.H., 1988a. Plastic deformation in nonstoichiometric UO<sub>2+x</sub> single crystals — II. deformation at high temperatures. *Acta Metall.* 36, 1073–1083. [https://doi.org/10.1016/0001-6160\(88\)90161-7](https://doi.org/10.1016/0001-6160(88)90161-7).
- Keller, R.J., Mitchell, T.E., Heuer, A.H., 1988b. Plastic deformation in nonstoichiometric UO<sub>2+x</sub> single crystals — I. deformation at low temperatures. *Acta Metall.* 36, 1061–1071. [https://doi.org/10.1016/0001-6160\(88\)90161-7](https://doi.org/10.1016/0001-6160(88)90161-7).
- Li, Y., Liang, T., Sinnott, S.B., Phillipot, S.R., 2013. A charge-optimized many-body potential for the U–UO<sub>2</sub>–O<sub>2</sub> system. *J. Phys. Condens. Matter* 25, 505401. <https://doi.org/10.1088/0953-8984/25/50/505401>.
- Lunev, A., Kuksin, A., Starikov, S., 2017a. Glide mobility of the 1/2[1 1 0](0 0 1) edge dislocation in UO<sub>2</sub> from molecular dynamics simulation. *Int. J. Plast.* 89, 85–95. <https://doi.org/10.1016/j.ijplas.2016.11.004>.
- Lunev, A., Zazolin, A., Pchelyakov, D., Grigoriev, E., Isaenkova, M., Perlovich, Y., Krymskaya, O., 2017b. On morphological and microstructural changes in uranium dioxide powder during binder-free hot pressing. *Defect Diffusion Forum* 375, 114–122. <https://doi.org/10.4028/www.scientific.net/DDF.375.114>.
- Marian, J., Cai, W., Bulatov, V.V., 2004. Dynamic transitions from smooth to rough to twinning in dislocation motion. *Nat. Mater.* 3, 158. <https://doi.org/10.1038/nmat1072>.
- Marlowe, M., 1969. High temperature isothermal elastic moduli of UO<sub>2</sub>. *J. Nucl. Mater.* 33, 242–244. [https://doi.org/10.1016/0022-3115\(69\)90064-6](https://doi.org/10.1016/0022-3115(69)90064-6).
- Morelon, N.D., Ghaleb, D., Delaye, J.M., Brutzel, L.V., 2003. A new empirical potential for simulating the formation of defects and their mobility in uranium dioxide. *Phil. Mag.* 83, 1533–1555. <https://doi.org/10.1080/1478643031000091454>.
- Murphy, S.T., Rushton, M.J., Grimes, R.W., 2014. A comparison of empirical potential models for the simulation of dislocations in uranium dioxide. *Prog. Nucl. Energy* 72, 27–32. <https://doi.org/10.1016/j.pnucene.2013.09.010>. symposium E @ E-MRS 2013 SPRING MEETING Scientific basis of the nuclear fuel cycle.
- Naamane, S., Monnet, G., Devincere, B., 2010. Low temperature deformation in iron studied with dislocation dynamics simulations. *Int. J. Plast.* 26, 84–92. <https://doi.org/10.1016/j.ijplas.2009.05.003>.
- Parfitt, D.C., Bishop, C.L., Wenman, M.R., Grimes, R.W., 2010. Strain fields and line energies of dislocations in uranium dioxide. *J. Phys. Condens. Matter* 22, 175004. <https://doi.org/10.1088/0953-8984/22/17/175004>.
- Petukhov, B., 2001. Statistical model of the local pinning of dislocations due to cross-slip events. *Mater. Sci. Eng. A* 309–310, 345–347. [https://doi.org/10.1016/S0921-5093\(00\)01714-7](https://doi.org/10.1016/S0921-5093(00)01714-7). *dislocations 2000*. An International Conference on the Fundamentals of Plastic Deformation.
- Plimpton, S., 1995. Fast parallel algorithms for short-range molecular dynamics. *J. Comput. Phys.* 117, 1–19. <https://doi.org/10.1006/jcph.1995.1039>. <http://lammps.sandia.gov/>.
- Po, G., Cui, Y., Rivera, D., Cereceda, D., Swinburne, T.D., Marian, J., Ghoniem, N., 2016. A phenomenological dislocation mobility law for bcc metals. *Acta Mater.* 119, 123–135. <https://doi.org/10.1016/j.actamat.2016.08.016>.
- Potashnikov, S.I., Boyarchenkov, A.S., Nekrasov, K.A., Kupryazhkin, A.Y., 2011. High-precision molecular dynamics simulation of UO<sub>2</sub>–PuO<sub>2</sub>: pair potentials comparison in UO<sub>2</sub>. *J. Nucl. Mater.* 419, 217–225. <https://doi.org/10.1016/j.jnucmat.2011.08.033>.
- Rao, S., Dimiduk, D., El-Awady, J., Parthasarathy, T., Uchic, M., Woodward, C., 2015. Screw dislocation cross slip at cross-slip plane jogs and screw dipole annihilation in FCC Cu and Ni investigated via atomistic simulations. *Acta Mater.* 101, 10–15. <https://doi.org/10.1016/j.actamat.2015.08.070>.
- Rodney, D., Provile, L., 2009. Stress-dependent peierls potential: influence on kink-pair activation. *Phys. Rev. B* 79, 094108. <https://doi.org/10.1103/PhysRevB.79.094108>.
- Sattonnay, G., Tetot, R., 2013. Bulk, surface and point defect properties in UO<sub>2</sub> from a tight-binding variable-charge model. *J. Phys. Condens. Matter* 25, 125403. <https://doi.org/10.1088/0953-8984/25/12/125403>.

- Scott, R., Hall, A., Williams, J., 1959. The plastic deformation of uranium oxides above 800 °C. *J. Nucl. Mater.* 1, 39–48. [https://doi.org/10.1016/0022-3115\(59\)90009-1](https://doi.org/10.1016/0022-3115(59)90009-1).
- Skelton, R., Walker, A.M., 2017. Peierls-Nabarro modeling of dislocations in  $\text{UO}_2$ . *J. Nucl. Mater.* 495, 202–210. <https://doi.org/10.1016/j.jnucmat.2017.08.024>.
- Soulacroix, J., Michel, B., Gatt, J.M., Kubler, R., Barrallier, L., 2014. An aging elasto-viscoplastic model for ceramics. *Int. J. Plast.* 62, 121–137. <https://doi.org/10.1016/j.ijplas.2014.07.006>.
- Soulié, A., Crocombette, J.P., Kraych, A., Garrido, F., Sattonnay, G., Clouet, E., 2018. Atomistically-informed thermal glide model for edge dislocations in uranium dioxide. *Acta Mater.* 150, 248–261. <https://doi.org/10.1016/j.actamat.2018.03.024>.
- Srivastava, K., Gröger, R., Weygand, D., Gumbsch, P., 2013. Dislocation motion in tungsten: atomistic input to discrete dislocation simulations. *Int. J. Plast.* 47, 126–142. <https://doi.org/10.1016/j.ijplas.2013.01.014>.
- Stukowski, A., 2010. Visualization and analysis of atomistic simulation data with OVITO — the open visualization tool. *Model. Simulat. Mater. Sci. Eng.* 18, 015012. <https://doi.org/10.1088/0965-0393/18/1/015012>. <http://ovito.org/>.
- Stukowski, A., Bulatov, V.V., Arsenlis, A., 2012. Automated identification and indexing of dislocations in crystal interfaces. *Model. Simulat. Mater. Sci. Eng.* 20, 085007. <https://doi.org/10.1088/0965-0393/20/8/085007>.
- Tseplyaev, V., Serenko, N., Starikov, S., 2017. The investigation of dislocation behaviour in molybdenum using molecular dynamics. *Defect Diffusion Forum* 375, 175–181. <https://doi.org/10.4028/www.scientific.net/DDF.375.175>.
- Wang, Z., Beyerlein, I., 2011. An atomistically-informed dislocation dynamics model for the plastic anisotropy and tension–compression asymmetry of BCC metals. *Int. J. Plast.* 27, 1471–1484. <https://doi.org/10.1016/j.ijplas.2010.08.011>. conventional and Emerging Materials.
- Yakub, E., Ronchi, C., Staicu, D., 2009. Computer simulation of defects formation and equilibrium in non-stoichiometric uranium dioxide. *J. Nucl. Mater.* 389, 119–126. <https://doi.org/10.1016/j.jnucmat.2009.01.029>.
- Yanilkina, A., Krasnikov, V., Kuksin, A., Mayer, A., 2014. Dynamics and kinetics of dislocations in Al and Al–Cu alloy under dynamic loading. *Int. J. Plast.* 55, 94–107. <https://doi.org/10.1016/j.ijplas.2013.09.008>.
- Yust, C., McHargue, C., 1969. Dislocation substructures in deformed uranium dioxide single crystals. *J. Nucl. Mater.* 31, 121–137. [https://doi.org/10.1016/0022-3115\(69\)90187-1](https://doi.org/10.1016/0022-3115(69)90187-1).
- Zhou, Q., Wang, J., Misra, A., Huang, P., Wang, F., Xu, K., 2016. Atomistic study of fundamental character and motion of dislocations in intermetallic  $\text{Al}_2\text{Cu}$ . *Int. J. Plast.* 87, 100–113. <https://doi.org/10.1016/j.ijplas.2016.09.005>.